Cancer Nanotechnology

RESEARCH Open Access

Induction of ferroptosis by artesunate nanoparticles is an effective therapeutic strategy for hepatocellular carcinoma

Dengyun Nie[1], Ting Guo[1], Xinyu Zong[1], Wenya Li[1], Yinxing Zhu[2], Miao Yue[1], Min Sha[2] and Mei Lin[1*]

*Correspondence: l_mei@163.com; linmei@njmu.edu.cn

[1] Taizhou People's Hospital affiliated to Chinese Medicine of Nanjing University, Taizhou 225300, Jiangsu, China
[2] Taizhou People's Hospital affiliated to Nanjing Medical University, Taizhou 225300, Jiangsu, China

Abstract

Artesunate (ART) has great value in the field of tumor therapy. Interestingly, in this study, we found that ART could obviously induce ferroptosis in hepatocellular carcinoma (HCC) cells, but its low water solubility and bioavailability limited its application potential. Hence, we synthesized ART-loaded mesoporous silica nanoparticles (MSNs) conjugated with folic acid (FA) (MSN-ART-FA) with tumor-targeting performance and assessed their characteristics. We evaluated the ability of MSN-ART and MSN-ART-FA to induce ferroptosis of hepatoma cells via testing levels of reactive oxygen species (ROS), Fe^{2+}, malondialdehyde (MDA) and glutathione (GSH), observation of mitochondrial morphology, as well as the expression of key proteins in ferroptosis. The results showed that prepared MSN-ART and MSN-ART-FA could remarkedly improve the bioavailability of ART to enhance ferroptosis, thereby inhibiting cell proliferation, migration and invasion in vitro. Besides, MSN-ART-FA group displayed slower tumor growth and smaller tumor volumes than MSN-ART group in HepG2 xenograft mouse model. It provided a potential therapeutic option for HCC and expanded the horizon for the clinical treatment of other cancers.

Keywords: Artesunate, Mesoporous silica nanoparticles, Hepatocellular carcinoma, Ferroptosis, Therapy

Graphical Abstract

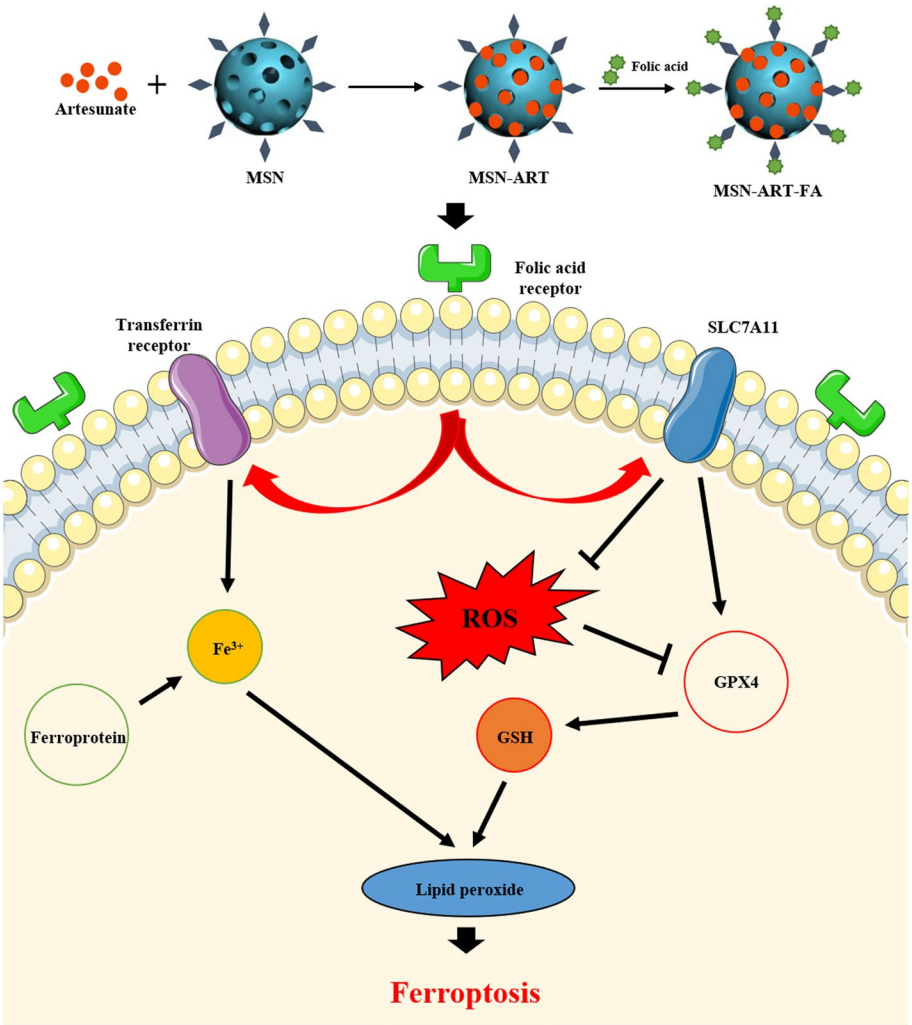

Introduction

Hepatocellular carcinoma (HCC) is the third leading cause of cancer-related death worldwide (Zhou et al. 2021). Although liver transplantation has been considered the most effective treatment for HCC, organ shortage severely limits the application of liver transplantation (Hwang et al. 2010). So far, chemotherapy remains the most commonly used treatment for patients with all stages of HCC. However, several first-line chemotherapeutic drugs for HCC, such as sorafenib and regorafenib, still have severe adverse reactions and drug resistance (Ikeda et al. 2018). Therefore, the development of potential chemotherapeutic drugs with few side effects and high efficacy for HCC is extremely valuable.

Traditional Chinese medicine has been applied in tumor prevention and treatment for over thousands of years owing to its low toxicity and high effectiveness. Artesunate

(ART) is a derivative of artemisinin, an effective anti-malaria monomer isolated from Artemisia annua in the 1970s (Chekem and Wierucki 2006). In addition to traditional anti-malarial effect of ART, several studies have shown that ART significantly inhibits the proliferation of tumor cells (Berköz et al. 2021; Yang et al. 2021). Additionally, the combination of ART and sorafenib has a synergistic enhancement effect on the growth inhibition of hepatoma cells, and can mutually promote the induction of apoptosis of hepatoma cells and inhibit the migration of hepatoma cells under a certain proportion of combined effects (Li et al. 2019).

As a newly discovered way of programmed cell death, ferroptosis are closely linked to the occurrence and progression of HCC (Capelletti et al. 2020). It has unique changes in morphology and metabolism different from apoptosis, autophagy and pyroptosis. In terms of morphology, ferroptosis is characterized by mitochondrial shrinkage and mitochondrial crista reduction. Up to now, it is generally believed that the main mechanism of ferroptosis is the depletion of glutathione (GSH) and the deactivation of glutathione peroxidase 4(GPX4), resulting in the metabolism of lipid peroxides cannot be achieved through the glutathione reductase reaction catalyzed by GPX4. Later, divalent iron ions oxidize the lipids to produce reactive oxygen species (ROS). When the production of ROS is excessive and the antioxidant capacity is insufficient, the balance between the production and removal of ROS breaks, which leads to ferroptosis of cells (Mou et al. 2019). Latest studies have indicated that ART can induce the ferroptosis of multifarious tumor cells (Wang et al. 2019; Eling et al. 2015; Song et al. 2022; Chen et al. 2021). Hepatoma cells contain a high concentration of free iron and ROS (Hu et al. 2021a, b; Lee et al. 2021). ART can react with free iron to generate free radicals to kill hepatoma cells (Bai et al. 2021a, b), which makes it a promising therapeutic drug for HCC. Nevertheless, ART has some disadvantages, such as poor oral bioavailability, poor water solubility and short half-life, which severely restrict its efficacy in clinic.

Nanomedicine with rapid development provides a bran-new method for reducing toxicity, improving bioavailability and tumor-targeting performance of chemotherapeutic drugs. Among various nanomedicine delivery platforms, mesoporous silica nanoparticles (MSNs) have become a research hotspot because of their great biocompatibility and high drug loading. However, the common MSNs as drug delivery system are not highly selective in tumor tissue, which still have poor efficacy. Fortunately, the negative charge on the surface of MSNs makes them easy to couple, which means that multifunctional MSNs can be prepared by coupling a variety of biomolecules such as drugs, targeting ligands, proteins and genes. The rapid elimination of the reticuloendothelial system (RES) will inevitably hinder the absorption efficiency of nanomaterials in the tumor area, resulting in low bioavailability of nanomedicine (Zhu et al. 2021). PEG with high hydrophilicity and positive charge is usually used to modify nanoparticles (Yang et al. 2020), in order to improve the biodistribution of nanoparticles and reduce opsonization by the RES (Tang et al. 2019a, b). Moreover, folic acid (FA) modified nanoparticles can bind to folic acid receptors (FRs) on various tumor cell membranes through FA ligands (Kumar et al. 2019; Farran et al. 2019), and then enter tumor cells to release their loaded drugs based on receptor-mediated endocytosis in order to improve bioavailability and targeting. Several studies on the development of FA complexes modified nanoparticles have

demonstrated their excellent tumor targeting both in vitro and in vivo (Tang et al. 2019a, b, 2020).

Thus, in this study, we firstly confirmed that ART had a strong ability to induce ferroptosis in hepatoma carcinoma cells. We further synthesized and conjugated FA-PEG modified MSNs with ART to develop a novel type of nanomedicine (MSN-ART-FA) for HCC therapy. We evaluated the efficacy of MSN-ART-FA in HCC by testing ferroptosis of hepatoma cells at the levels of animal, cell and molecular, which also broadened the horizon for the clinical treatment of other tumors.

Materials and methods

Reagents

ART was purchased from Yuanye Biotech (S24000, Shanghai, China). Monodisperse PEG-modified MSNs were provided by Nanoeast Biotech (HMSNs-PEG, Nanjing, China). PEG-modified folic acid (FA) (R-1209-2k) and Cy5.5 NHS ester (R-FR-005) were purchased from Ruixi Biotech (Xian, China). EDC (T511307) and NHS (130,672) were purchased from Sigma (America). Trolox (GC19457), ferrostatin-1 (Fer-1) (GC10380), liproxstatin-1 (Lip-1) (GC15681), and erastin (GC16630) were purchased from GLPBIO (America). Desferrioxamine (DFO) (HY-B0988) were purchased from MedChemExpress (America). The CCK-8 assay kit (C0042), ROS assay kit (S0033M), MDA assay kit (S0131M) and GSH assay kit (S0053) were purchased from Beyotime (Shanghai, China). Additionally, the iron content assay kit (BC5415) was purchased from Solarbio (Beijing, China). Antibodies against TFRC (# 13,113 S), SLC7A11 (# 12,691 S), GPX4 (# 59,735 S), FTH1 (# 4393 S) and Tubulin (# 2128 S) were purchased from Cell Signaling Technology (America). HRP-conjugated Mouse anti-rabbit IgG (# ab6721) was purchased from Abcam (Britain).

Preparation of the nanoparticles

The MSN-PEG-NH2-Cy5.5-ART (abbreviation: MSN-ART) was prepared according to our previous method in the published paper(Zhu et al. 2021). Briefly, 5 mg MSN-PEG-NH2 (10 mg/mL), 500 μg ART (10 mg/mL) and 100 μg Cy5.5 (5 mg/mL) were mixed evenly in ethanol. Under ultrasonic condition, 100 μL water droplets were added to the above solution, and ethanol was added to the volume of 1mL. The samples were then incubated in a 37 ℃ shaker for 20 h. Finally, the free ART and Cy5.5 were removed by centrifugal washing (10,000 rpm, 15 min) to obtain the required samples, which were then vacuum dried at 45 ℃ for 12 h and then stored at 4 ℃.

The MSN-PEG-NH2-Cy5.5-ART-FA (abbreviation: MSN-ART-FA) was further prepared based on the MSN-PEG-NH2-Cy5.5-ART. 5 mg MSN-PEG-NH2-Cy5.5-ART (5 mg/mL) was washed and fixed volume to 1 mL with PB solution (20 mM, pH = 7.4). Additionally, FA-PEG-COOH was dissolved in CB solution (10 mM, pH = 9.0) and EDC was dissolved in MES solution (15 mM, pH = 5.5). 2.5 mg FA-PEG-COOH (5 mg/mL) and 5 mg EDC (10 mg/mL) were added in MSN-PEG-NH2-Cy5.5-ART solution, then the mixture was fixed volume to 5 mL in volume with MES solution,

incubated at 37 ℃ for 20 h. The same centrifugal washing, drying and storing steps were conducted to obtain the MSN-PEG-NH2-Cy5.5-ART-FA.

High performance liquid chromatography (HPLC)

The ART residue in foregoing sample solution was determined by HPLC to assess the ART loading in nanoparticles. The chromatographic conditions were as follows: WondaSil C18 column. The mobile phase used was acetonitrile: water (dilute acetic acid to pH 4.5) = (55:45). The flow rate of mobile phase was set at 1.0 mL/min. The column was maintained at 30 ℃ and detected at 210 nm. Meanwhile, ART standard solution (1 mg/mL) in acetonitrile was prepared and stored it at − 20 °C.

1 mL MSN-ART solution (1 mg/mL) was added into the dialysis bag (MW: 3500) and into a centrifuge tube containing 5 mL PBST buffer (pH = 7.4, 0.2% Tween-80). The centrifuge tube was placed on a constant temperature shaker at 37 ℃ and 100 rpm, which was sheltered from light. At 1, 6, 12 and 24 h, 1 mL of release liquid was taken from the centrifuge tube, and then it was put into the sample tube to be measured. PBS buffer solution (pH = 7.4) at the same temperature was randomly added into the centrifuge tube for further shock. The ART content of the released liquid extracted at each time period was tested by HPLC. The release concentration of ART in dialysis bags in different time periods was calculated, and the cumulative release curve was drawn with time as the abscissa and the cumulative release percentage as the ordinate.

Characterization of the nanoparticles

The physical and chemical properties of nanoparticles were characterized by transmission electron microscopy (TEM) (TecnaiG20, USA) and dynamic light scattering (DLS) (DynaPro NanoStar, USA) with reference to our published paper (Zhu et al. 2021). TEM was used to observe the shapes of the nanoparticles, and DLS was applied in testing the hydrodynamic diameter and Zeta potential of the nanoparticles. Additionally, we used Fourier transform micro-infrared spectrometer (Thermo Scientific Nicolet iN10, America) to determine the infrared absorption condition of samples with potassium bromide tablets, 4000 ~ 400 cm^{-1} range scan.

Cell culture

The human HepG2 and Huh7 hepatocellular cancer cell lines and HL-7702 hepatocytes were obtained from the Shanghai Institute of Cell Research, Chinese Academy of Sciences (Shanghai, China). HepG2 cells were cultured in MEM (GIBCO, America) containing 15% fetal bovine serum (GIBCO, America) and Huh7 cells were cultured in DMEM (GIBCO, America) containing 10% fetal bovine serum. HL-7702 hepatocytes were cultured in 1640 (GIBCO, America) containing 10% fetal bovine serum. All cells were supplemented with streptomycin and penicillin (GIBCO, America), and were cultured at 37 ℃ in a humidified environment with 5% CO_2.

Animal experiments

Five-week-old female BALB/c-Nude mice were purchased from Jiangsu Huachuang Xinuo Medical Technology Co., LTD (Taizhou, Jiangsu). HepG2 cells were collected and resuspended in PBS at a concentration of $1 \sim 5 \times 10^7$ cells/mL. 0.1 mL of the cell suspension was inoculated subcutaneously in the middle armpits of mice. After confirming tumor formation, the mice received local injection of saline, MSN, ART, MSN-ART and MSN-ART-FA in accordance with the body weight (ART: 20 mg/kg) daily. The diameter of the transplanted tumor was measured using a Vernier caliper every two days. Fifteen days later, the mice were killed. Tumor volume was calculated according to the following formula: $V = (a \times b^2)/2$ ('a' is long axis, 'b' is short axis).

Six-week-old male C57BL/6J mice were purchased from Jiangsu Huachuang Xinuo Medical Technology Co., LTD. The mice were randomly divided into five groups and they received daily saline, MSN, ART, MSN-ART or MSN-ART-FA treatments in accordance with the body weight (ART: 100 mg/kg) for one week, respectively. Seven days later, the mice were killed for follow-up experiments.

All mice used in the experiments were group-housed in a temperature-controlled environment and provided access to food and water. All behavioral procedures were performed during the light cycle. According to the International Society for the Study of Cancer guidelines, we attempted to use the minimum number of mice necessary to achieve statistical significance.

Cell viability

Cell viability was determined using a CCK-8 assay (Beyotime, Shanghai, China). Briefly, $1 \sim 3 \times 10^4$ HepG2, Huh7 or HL-7702 cells/well were seeded into 96-well plates and treated with experimental agents. Following intervention for 24 h, 10 μl CCK-8 reagent was added to each well and incubated at 37 ˚C for a further 30 min, according to the manufacturer's protocol. Finally, the absorbance was measured using a microplate reader (BioTek, America) at a wavelength of 450 nm. The cell viability rate was calculated according to the formula: cell viability rate (%) = (experimental absorbance value-blank absorbance value) / (control absorbance value-blank absorbance value) × 100.

Determination of iron, ROS, malondialdehyde (MDA), and intracellular GSH content

The iron content was determined according to the iron content assay kit instructions (Solarbio, Beijing, China) using a microplate reader (BioTek, America). The ROS level was detected in accordance with the instructions of the ROS assay kit (Beyotime, Shanghai, China) using the fluorescence microscope (Leica, Germany) and flow cytometry (Beckman Coulter, America). MDA content and intracellular GSH content were measured according to the manufacturer's instructions provided by the kits (Beyotime, Shanghai, China) by aforesaid microplate reader.

Western blot

Cells or tumors lysates were prepared in RIPA buffer with proteinase inhibitors (Beyotime, Shanghai, China). The equal amount of protein from each sample was added into the SDS-PAGE gel for electrophoresis. After electrophoresis, all protein were transferred from the gel to a PVDF membrane (Millipore, America). The PVDF membrane was then

sealed and exposed to the corresponding antibody. All antibodies are described above. The blots were visualized by enhanced chemiluminescence (Vazyme Biotech, Shanghai, China), and digital images and densitometry were performed using the G: BOX Chemi XX9 imaging system (Syngene, Britain).

Cellular uptake of nanoparticles in vitro

HepG2 and Huh7 cells in the logarithmic growth phase were, respectively, seeded in 6-well plates at 5×10^5 cells per well and cultured overnight. All cells were exposed to DAPI for 15 min and then washed with PBS three times. Subsequently, MSN-ART-Cy5.5 and MSN-ART-FA-Cy5.5 were, respectively, added into the wells (equal to 5 μg/mL in the medium) and incubated for 2 h. After washing with PBS, the fluorescence signal of nanomedicine in cells was observed under a fluorescence microscope (Leica, Germany). The mean rate of merge was quantified with ImageJ.

Wound healing assay

HepG2 cells were cultured in a 12-well plate with 2×10^5 cells per well until the dishes were completely covered. The cell layer was wounded using a sterile 200-μL tip and washed with PBS, and then cultured with serum-free medium for 24 h. The diffusion of wound closure at different time points (0 and 24 h) was observed under a microscope (Leica, Germany), and photographs were taken to assess the migration distance.

Transwell invasion assays

After saline or ART intervention, 1×10^5 cells were suspended in the upper compartment with 200 μL serum-free medium and 600 μL complete medium was added into the lower compartment. The matrigel (Becton Dickinson, America) was between upper compartment and lower compartment. The invasive cells migrated to the lower compartment and were stained with crystal violet (Solarbio, Beijing, China) after 24 h. Three visual fields were selected at random from each compartment and counted under the microscope (Leica, Germany).

Histopathological observation

After fixation in 10% neutral formaldehyde solution, all tissues were routinely paraffin-embedded, then sliced into 5-μm sections. Pathological changes in all tissues were observed under a microscope (Leica, Germany) after routine hematoxylin and eosin (H&E) staining.

Blood and biochemical analysis

Tail vein blood was extracted from all mice after treatment. The changes in red cells, white cells, hemoglobin and platelets in the blood were detected using animal blood analyzer (pocH-100i, SYSMEX, Japan). Similarly, the levels of alanine transaminase (ALT), aspartate aminotransferase (AST), urea nitrogen (BUN) and

creatinine (Cr) in serum were tested via automatic biochemical analyzer (BC-5000 Vet, Mindray Medical, China).

Statistical analysis

Each experiment was performed in triplicate and data were shown as mean ± SEM. Comparisons between two groups were performed by Student's *t*-test, multigroup

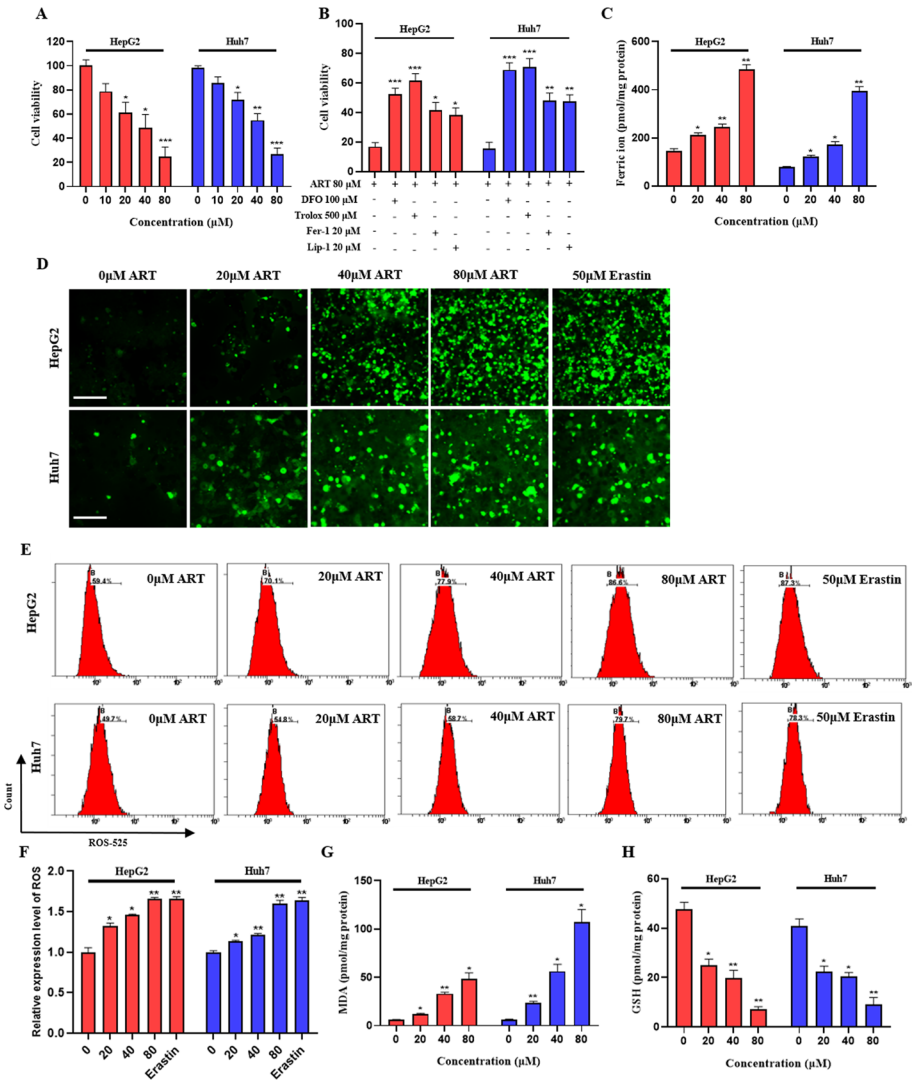

Fig. 1 ART induced ferroptosis in HepG2 and Huh7 cells. **A** Cell viability of HepG2 and Huh7 cells exposed to 0, 10, 20, 40 or 80 μM ART for 24 h. ($n = 5$ per group, $^{*}P < 0.05$, $^{**}P < 0.01$, $^{***}P < 0.001$). **B** Cell viability of HepG2 and Huh7 cells treated with 100 μM DFO, 500 μM Trolox, 20 μM Lip-1 or 20 μM Fer-1, and then exposed to 80 μM ART for 24 h. ($n = 5$ per group, $^{*}P < 0.05$, $^{**}P < 0.01$). **C** Iron content in HepG2 and Huh7 cells exposed to 0, 20, 40 or 80 μM ART for 24 h. ($n = 3$ per group, $^{*}P < 0.05$, $^{**}P < 0.01$). **D** Fluorescence images (scale bar: 50 μm) and **E** fluorescence signal intensity of ROS in HepG2 and Huh7 cells exposed to 0, 20, 40, 80 μM ART or 50 μM erastin for 24 h. **F** ROS level of HepG2 and Huh7 cells exposed to 0, 20, 40, 80 μM ART or 50 μM erastin for 24 h. ($n = 3$ per group, $^{*}P < 0.05$, $^{**}P < 0.01$). **G** MDA content and **H** GSH content in HepG2 and Huh7 cells exposed to 0, 20, 40, 80 μM ART for 24 h. ($n = 3$ per group, $^{*}P < 0.05$, $^{**}P < 0.01$). Bars indicate mean ± SEM

comparisons were performed using one-way ANOVA (version 8.0 GraphPad Prism, San Diego, CA, USA). $p < 0.05$ was considered as statistically significant.

Results

ART induced ferroptosis to suppress hepatoma carcinoma cells proliferation

To assess the cytotoxicity of ART for the HepG2 and Huh7 cells, we treated the HepG2 and Huh7 cells of proliferative phase with ART at different concentrations for 24 h. CCK8 assays showed that ART reduced the viability of hepatoma cells in a dose-dependent manner (Fig. 1A). After 24 h of treatment, the IC50 of ART was approximately 32.95 μM for HepG2 cells and 41.88 μM for Huh7 cells. We selected 20, 40 and 80 μM ART for 24 h in subsequent experiments. Meanwhile, ferroptosis inhibitors (DFO, Trolox, Lip-1, and Fer-1) all significantly weakened the inhibition effect of ART on the proliferation of the HepG2 and Huh7 cells (Fig. 1B), which suggested that ART induced ferroptosis in hepatoma carcinoma cells.

Considering that ferroptosis depends on the enrichment of iron, increased lipid ROS generation and decreased antioxidant enzymes, we tested the level of Fe^{2+}, ROS, MDA, GSH in the HepG2 and Huh7 cells treated with 20, 40 and 80 μM ART for 24 h by kits. As expected, experimental results showed that ART-induced ferroptotic phenotypes including Fe^{2+} accumulation (Fig. 1C), excessive production of ROS (Fig. 1D–F) and MDA (Fig. 1G), and exhausted GSH (Fig. 1H) still in a dose-dependent manner. As shown in transmission electron microscope photographs, mitochondrial volume decreased, mitochondrial crest disappeared and outer membrane fractured after 80 μM ART treatment (Fig. 2A).

To further reveal that ART induced ferroptosis in hepatoma carcinoma cells, we then assessed key regulatory protein of ferroptosis. Western blotting results (Fig. 2B, C) showed that ART treatment significantly enhanced the expression of TFRC in the HepG2 and Huh7 cells. The protein levels of SLC7A11, GPX4 and FTH1 were significantly downregulated by ART at the same time. In conclusion, these data showed that ART induced ferroptosis to suppress the proliferation of hepatoma carcinoma cells.

Characterization of nanoparticles

TEM observation was performed to display the morphological characteristics of MSN, MSN-ART and MSN-ART-FA (Fig. 3A–C). It could be seen that the nanoparticles all had regular spherical shapes, uniform particle sizes and great monodispersities before and after modification. Additionally, the nanoparticles maintained the basic morphology after surface modification, but the surface mesoporous channels became blurred. White halos appeared around the nanoparticles, corresponding to the modified polymer layer. MSN, MSN-ART and MSN-ART-FA all had the size of about 50 nm. According to the enhanced permeability and retention (EPR) effect, nanoparticles with a particle size of less than 100 nm easily passed through the space of tumor tissue, thus remaining in the tumor tissue (Park et al. 2016), especially the nanoparticles 50-100 nm in size have the ability of targeting to the liver (Hu et al. 2021a, b), which means that prepared MSN-ART and MSN-ART-FA were suitable for HCC treatment.

As shown in DLS assessment, MSN had a hydrodynamic size of 70 nm and a zeta potential of 45.2 mV (Fig. 3D, G). With the gradual modification of the MSNs with Cy5.5,

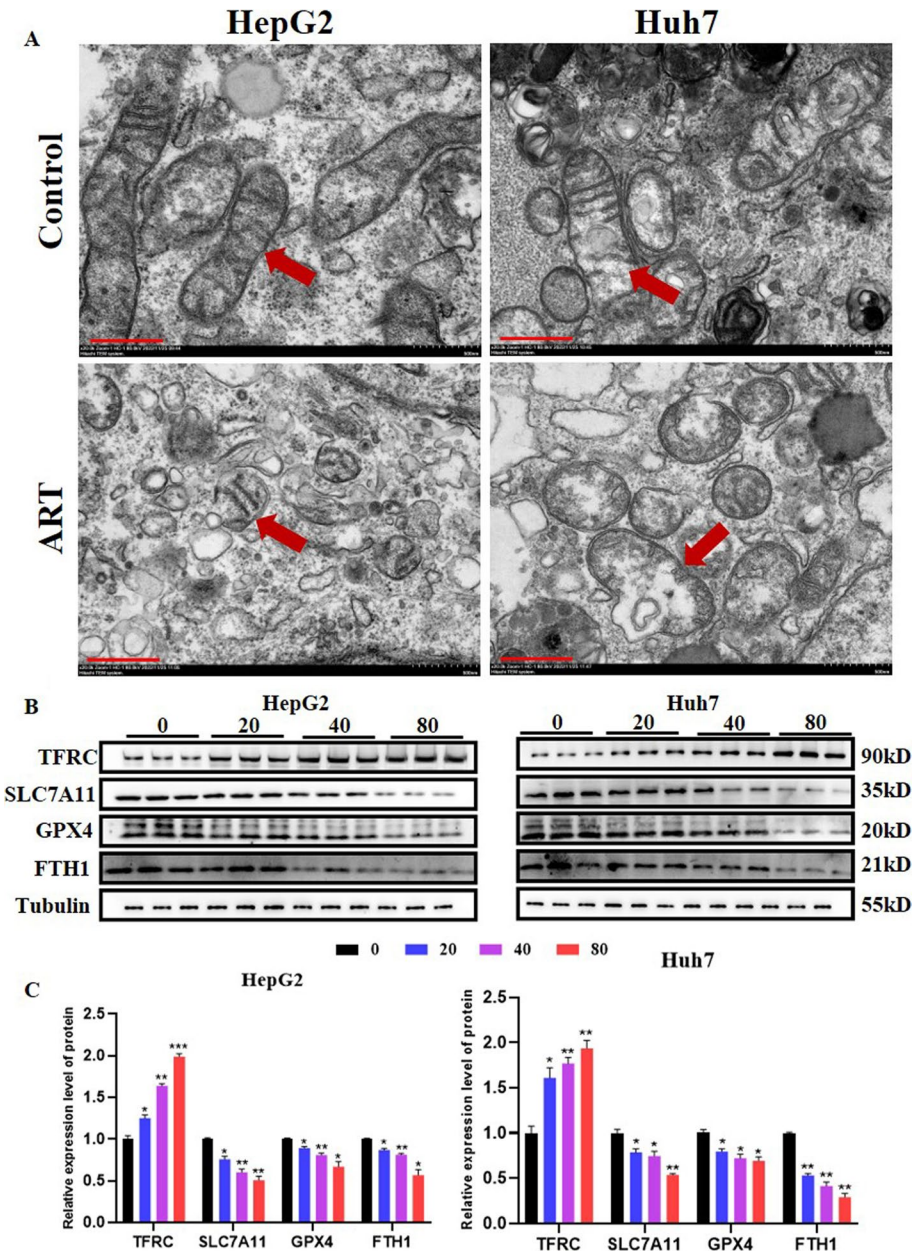

Fig. 2 Ultrastructure of mitochondria and regulation of key proteins associated with ART-induced ferroptosis. **A** Representative transmission electron microscope photographs of mitochondria in HepG2 and Huh7 cells treated for 24 h with 0 or 80 μM ART (scale bar: 500 nm). **B** Representative immunoblots and **C** graphic representation of relative expression of TFRC, SLC7A11, GPX4, FTH1 and Tubulin in HepG2 and Huh7 cells exposed to 0, 20, 40, 80 μM ART for 24 h. ($n = 3$ per group, $^{*}P < 0.05$, $^{**}P < 0.01$, $^{***}P < 0.001$). Bars indicate mean ± SEM

ART and FA, the MSN-ART and MSN-ART-FA showed increases in the hydrodynamic size separately to 74 and 80 nm (Fig. 3E–F). The HPLC data showed that the efficiency of MSN loaded ART was 7.88% (Additional file 1: Fig. S1 and Table S1). Besides, the surface charges of MSN-ART and MSN-ART-FA were 45.7 mV and −14.6 mV (Fig. 3H, I). As

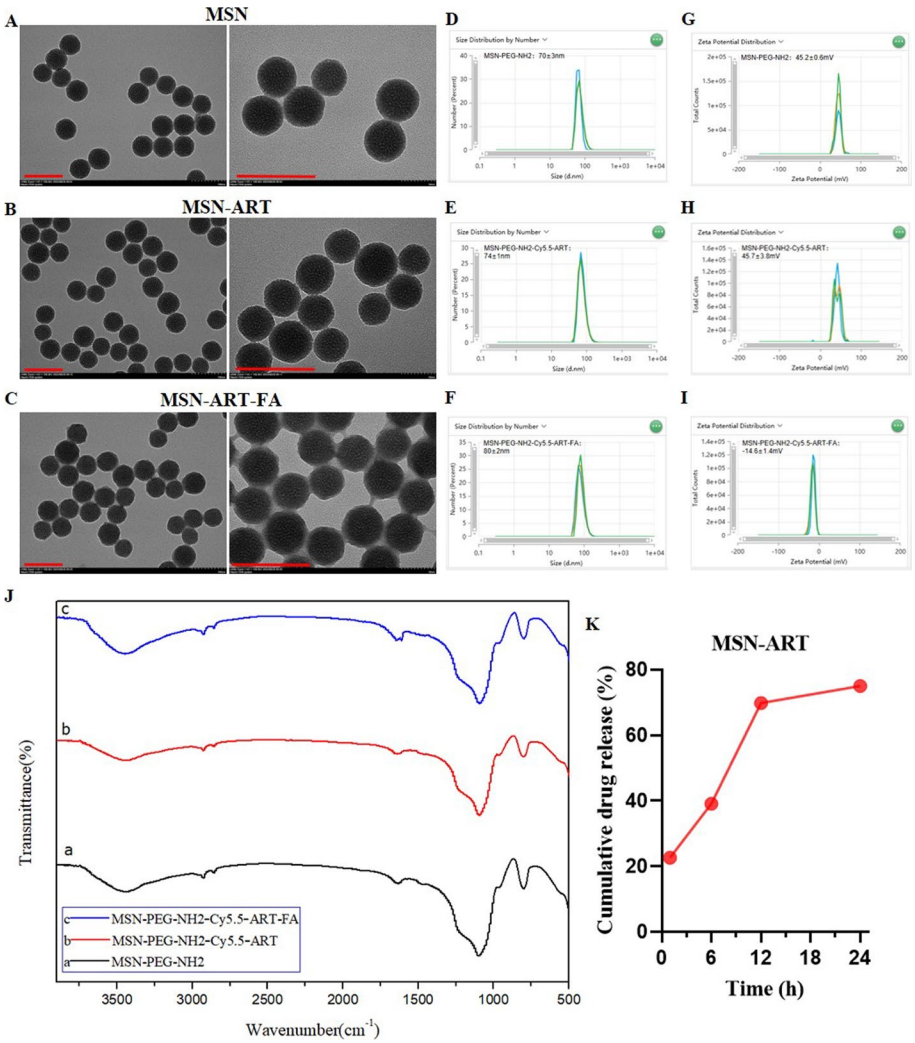

Fig. 3 Characterization of nanoparticles. Representative morphological features of **A** MSN, **B** MSN-ART and **C** MSN-ART-FA (Scale bar: 100 nm). Size distributions of **D** MSN, **E** MSN-ART and **F** MSN-ART-FA. Zeta potentials of **G** MSN, **H** MSN-ART and **I** MSN-ART-FA. **J** Infrared spectroscopies of MSN, MSN-ART and MSN-ART-FA. **K** In vitro release curve of MSN-ART at 1, 6, 12 and 24 h

expected, the surface charge of MSN-ART changed from positive to negative after FA coupling, indicating the successful modification of nanoparticles.

In the infrared spectrum of MSN-PEG-NH2 (Fig. 3J), the maximum absorption peak at 1098 cm^{-1} is the anti-symmetric stretching vibration of Si–O–Si bond. At 801 cm^{-1} and 466 cm^{-1}, there were symmetric stretching vibration and bending vibration of Si–O–Si bond, respectively. The absorption peaks near 965 cm^{-1} and 3445 cm^{-1} were the bending vibration absorption peaks of Si–OH and the anti-symmetric stretching vibration peaks, respectively. The absorption peaks at 1503 cm^{-1} and 1639 cm^{-1} were characteristic peaks of amino and amide bonds. The absorption peak at 2927 cm-1 is the characteristic peak of the methylene repeat unit in polyethylene glycol. All the characteristic peaks of MSN-PEG-NH2 still existed, but the intensity of the peaks changed after loading Cy5.5 and ART. After PEG-FA coupling, in addition to containing all the

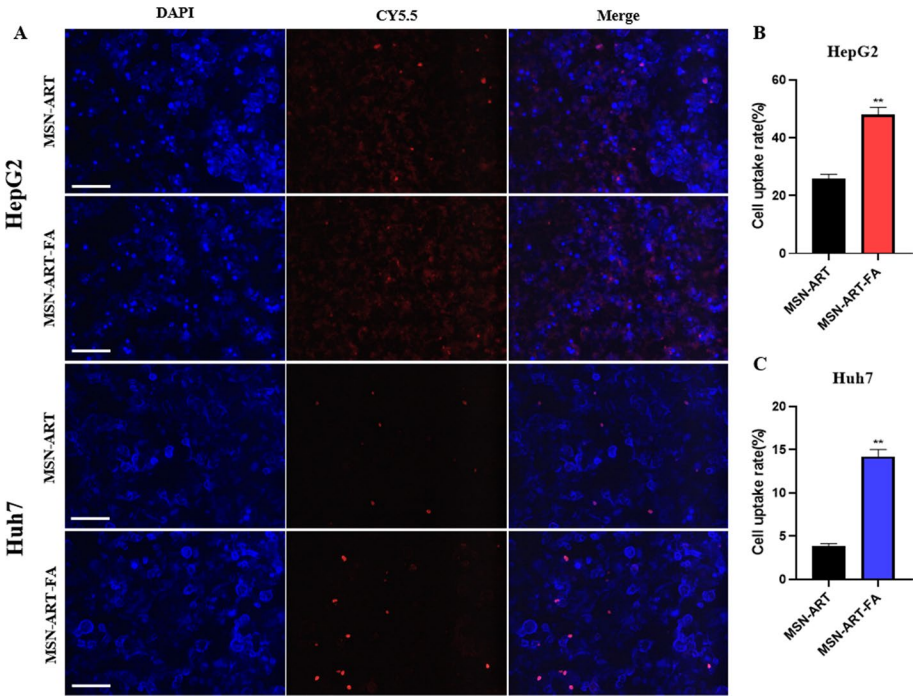

Fig. 4 Cellular uptake of MSN-ART-Cy5.5 and MSN-ART-FA-Cy5.5. **A** Representative fluorescence images of HepG2 and Huh7 cells exposed to MSN-ART-Cy5.5 and MSN-ART-FA-Cy5.5 for 2 h (scale bar: 50 μm). Graphic representation of cellular uptake of MSN-ART-Cy5.5 and MSN-ART-FA-Cy5.5 in **B** HepG2 and **C** Huh7 cells. ($n = 3$ per group, $^{**}P < 0.01$). Bars indicate mean ± SEM

characteristic peaks in MSN-PEG-NH2, the peak intensity of methylene absorption peak in PEG at 2927 cm^{-1} and that of amide bond at 1639 cm^{-1} increased, while a new peak appeared at 1610 cm^{-1}, which was attributed to the stretching vibration of benzene ring. These results showed that FA was successfully coupled on the surface of MSN-ART.

According to the in vitro release curve of MSN-ART (Fig. 3K), the ART was released slowly in the first 6 h. By 6 h, the release amount reached approximately 39.07%. With the extension of time, the cumulative release of the drug showed a trend of gradual increase. After 12 h, the release of ART was close to equilibrium, and the maximum release reached about 75.04%.

In the cellular uptake assay, it can be seen that the cellular uptake rate of MSN-ART-FA was significantly higher than that of MSN-ART both in HepG2 and Huh7 cells (Fig. 4A, B). This meant MSN-ART-FA was more targetable to hepatoma carcinoma cells. The mean cellular uptake rate of MSN-ART group and MSN-ART-FA group was 25.76 ± 1.679 and 48.02 ± 2.515 in HepG2 cells (Fig. 4B), however, that of MSN-ART group and MSN-ART-FA group was only 3.865 ± 0.2795 and 14.22 ± 0.8262 in Huh7 cells (Fig. 4C). In view of the higher cellular uptake rate of MSN-ART and MSN-ART-FA in HepG2 cells, we used HepG2 cells for follow-up experiments.

MSN-ART and MSN-ART-FA enhanced ART-induced ferroptosis in HepG2 cells

Next, we evaluated the effects of MSN-ART and MSN-ART-FA on HepG2 cell viability at the same dose of ART (IC50: 32.95 μM). The experimental results showed that MSN group had no significant effects on the viability of HepG2 cells compared to

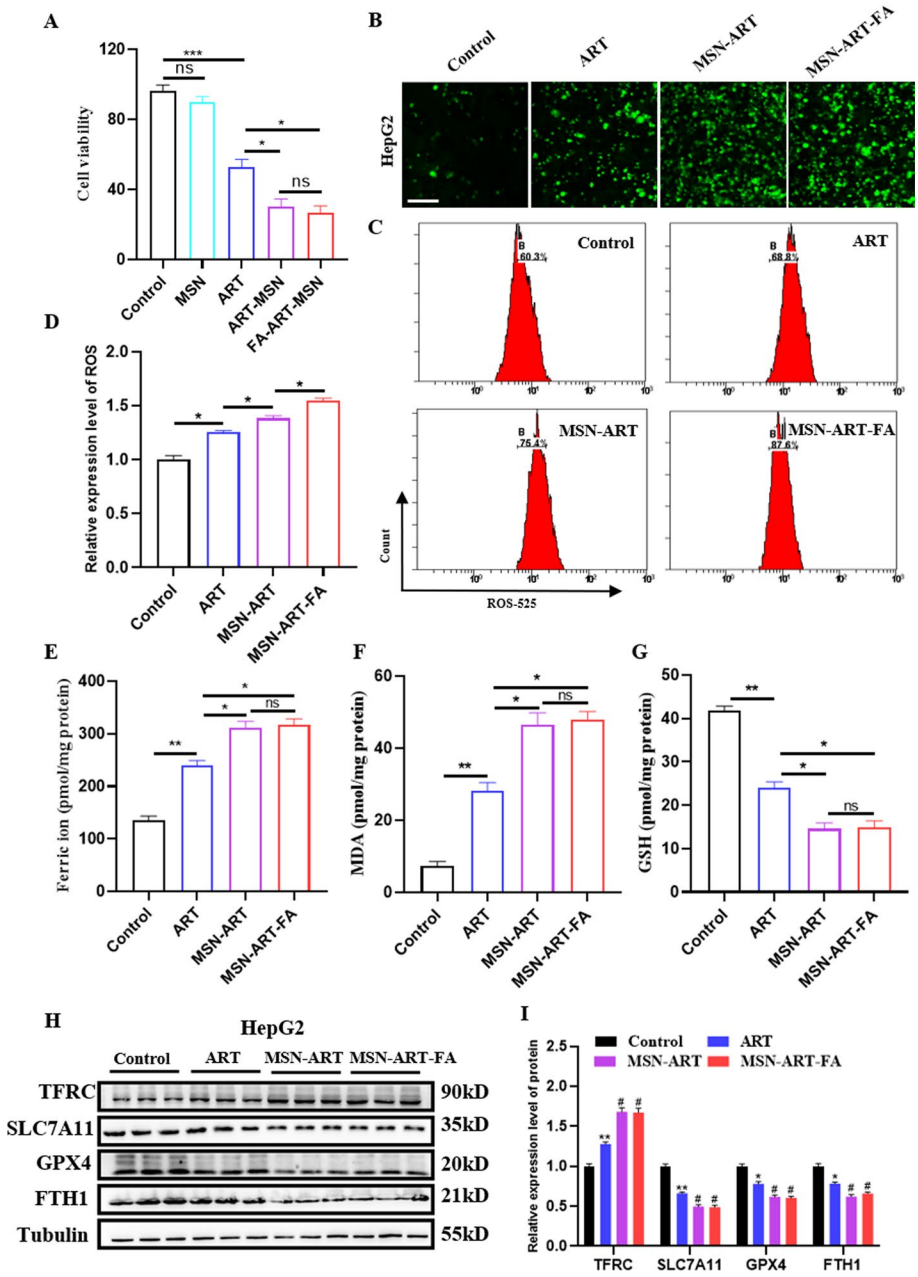

Fig. 5 MSN-ART and MSN-ART-FA enhanced ART-induced ferroptosis in HepG2 cells. **A** Cell viability of HepG2 cells exposed to saline, MSN, ART, MSN-ART or MSN-ART-FA for 24 h. ($n = 5$ per group, $^{*}P < 0.05$, $^{***}P < 0.001$). **B** Fluorescence images (Scale bar: 50 μm) and **C** fluorescence signal intensity of ROS in HepG2 cells exposed to exposed to saline, ART, MSN-ART or MSN-ART-FA for 24 h. **D** ROS level of HepG2 cells exposed to saline, ART, MSN-ART or MSN-ART-FA for 24 h. (n = 3 per group, $^{*}P < 0.05$). **E** Iron content, **F** MDA content and **G** GSH content in HepG2 cells exposed to saline, ART, MSN-ART or MSN-ART-FA for 24 h. ($n = 3$ per group, $^{*}P < 0.05$, $^{**}P < 0.01$). **H** Representative immunoblots and **I** graphic representation of relative expression of TFRC, SLC7A11, GPX4, FTH1 and Tubulin in HepG2 cells exposed to saline, ART, MSN-ART or MSN-ART-FA for 24 h. ($n = 3$ per group, $^{*}P < 0.05$, $^{**}P < 0.01$ compared to control, $^{\#}P < 0.05$ compared to ART). Bars indicate mean ± SEM

control group, and MSN-ART group and MSN-ART-FA group significantly inhibited cell viability compared to simple ART treatment group. Nevertheless, there was no clear difference in HepG2 cell viability between MSN-ART group and MSN-ART-FA group (Fig. 5A). Meanwhile, the iron content (Fig. 5E), MDA content (Fig. 5F), GSH content (Fig. 5G) of MSN-ART group and MSN-ART-FA group were significantly more than that of ART group, and there was no obvious difference between MSN-ART group and MSN-ART-FA group, which was consistent with our cell viability result. Unexpectedly,

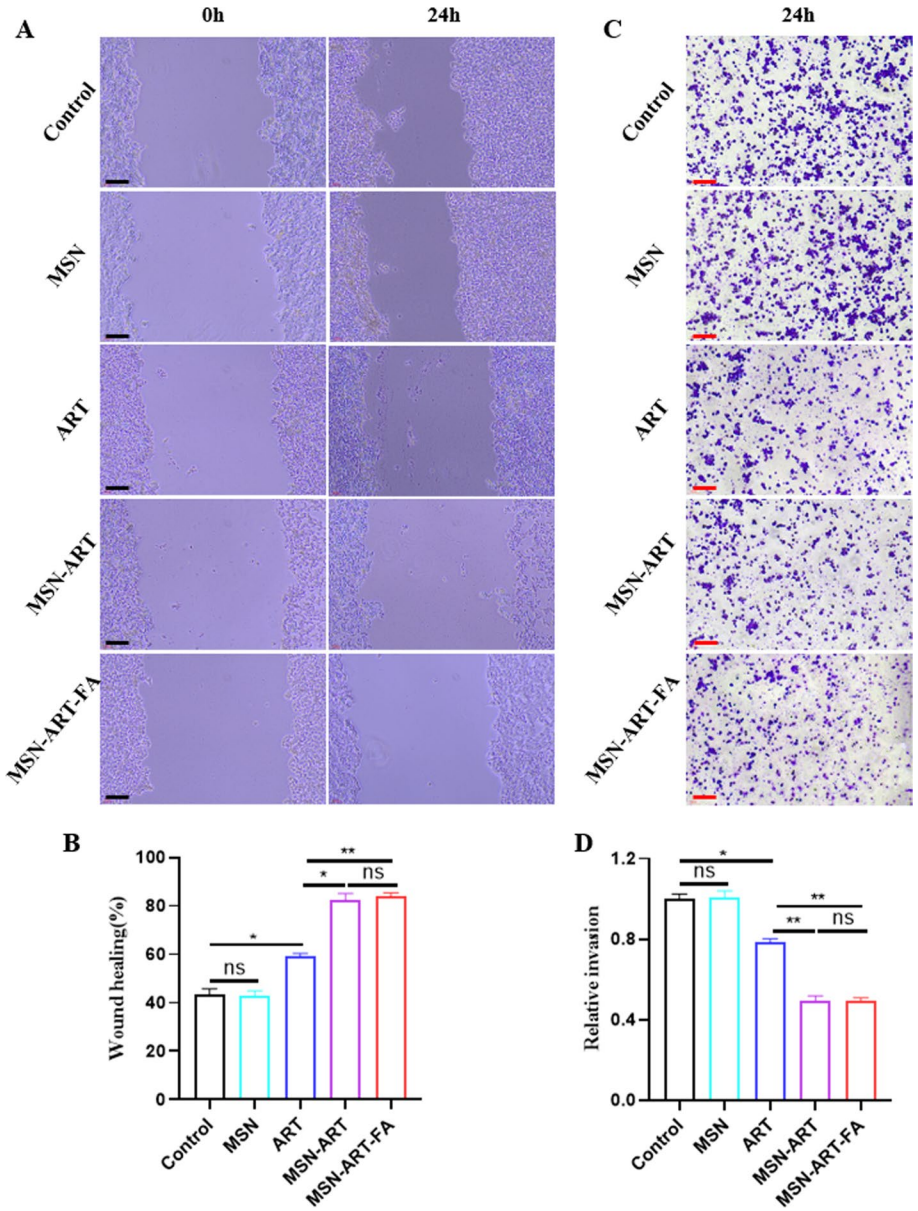

Fig. 6 MSN-ART and MSN-ART-FA inhibited the ability of HepG2 cells to migrate and invade. **A** Representative images (Scale bar: 100 μm) and **B** graphic representation of scratch wound healing assay in HepG2 cells exposed to saline, MSN, ART, MSN-ART or MSN-ART-FA for 24 h. ($n = 3$ per group, $^{*}P < 0.05$, $^{**}P < 0.01$). **C** Representative images (Scale bar: 100 μm) and **D** graphic representation of transwell assay in HepG2 cells exposed to saline, MSN, ART, MSN-ART or MSN-ART-FA for 24 h. ($n = 3$ per group, $^{*}P < 0.05$, $^{**}P < 0.01$). Bars indicate mean ± SEM

we found the ROS level of MSN-ART-FA group was significantly higher than that of MSN-ART group (Fig. 5B–D). In addition, MSN-ART group and MSN-ART-FA group markedly enhanced the expression of TFRC, and decreased the expression of SLC7A11, GPX4 and FTH1 (Fig. 5H, I). Based on the above results, MSN-ART and MSN-ART-FA enhanced ART-induced ferroptosis in HepG2 cells.

We then assessed the role of MSN-ART and MSN-ART-FA in the migration and invasion ability of HepG2 cells by wound healing assay and transwell invasion assay (Fig. 6). MSN group still had no evident effects on the migration and invasion ability of HepG2 cells compared to control group. ART group remarkably restrained cell migration at the edge of exposed regions (Fig. 6A, B) and decreased invasive HepG2 cells (Fig. 6C, D) compared to control group, and MSN-ART group and MSN-ART-FA group significantly enhanced this inhibitory effect of ART in the migration and invasion ability, whereas MSN-ART-FA group had no clear difference from MSN-ART group (Fig. 6B, D). These results suggested ART treatment exerted certain anti-HCC effects, and MSN-ART and MSN-ART-FA could improve this efficacy.

MSN-ART and MSN-ART-FA improved anti-HCC activity of ART in vivo

The in vivo anti-HCC efficacy of ART, MSN-ART and MSN-ART-FA was evaluated in the nude mice bearing subcutaneous inoculated HepG2 cells. Each mouse received a daily dose of ART equivalent to 20 mg/kg. Compared with control group, ART group significantly retarded tumor growth and reduced the size of the tumor nodules, which showed good anti-HCC efficacy. MSN-ART group had greater anti-HCC efficacy compared to ART group, and MSN-ART-FA group further improved this anti-HCC efficacy of MSN-ART group. MSN group showed negligible tumor inhibition, thus indicating that the increased bioavailability of ART played a major role rather than MSN alone in the improved efficacy of MSN-ART group and MSN-ART-FA group (Fig. 7A, B). More importantly, H&E pathological staining (Fig. 7C) revealed that ART group caused HepG2 cell death as evidenced by smeared cell morphology and the formation of cellular vacuoles, and MSN-ART group and MSN-ART-FA group caused more extensive cell death.

Additionally, the experimental results indicated that the content of iron (Fig. 7F), MDA (Fig. 7G) and GSH (Fig. 7H) in MSN-ART group and MSN-ART-FA group were markedly more than that in ART group, which was in keeping with the trend of efficacy. Interestingly, ART group and MSN-ART group seem to increase the level of ROS compared to control group, whereas there was no obvious difference among them, and only MSN-ART-FA group was able to notably increase ROS level compared to control group (Fig. 7D, E). We still assessed before-mentioned regulatory protein of ferroptosis (Fig. 7I) and found MSN-ART group significantly increased the expression of TFRC and decreased the expression of SLC7A11, GPX4 and FTH1. FA modification magnified the regulation of above protein by MSN-ART group (Fig. 7J). In brief, MSN-ART group and MSN-ART-FA group exhibited better anti-HCC effects at least in part via enhancing ART-induced ferroptosis in vivo.

Finally, we also observed the pathological changes in the main organs of the nude mice after the intervention of MSN, ART, MSN-ART and MSN-ART-FA, and we found they were not significantly different in heart lung, liver, kidney and spleen compared to

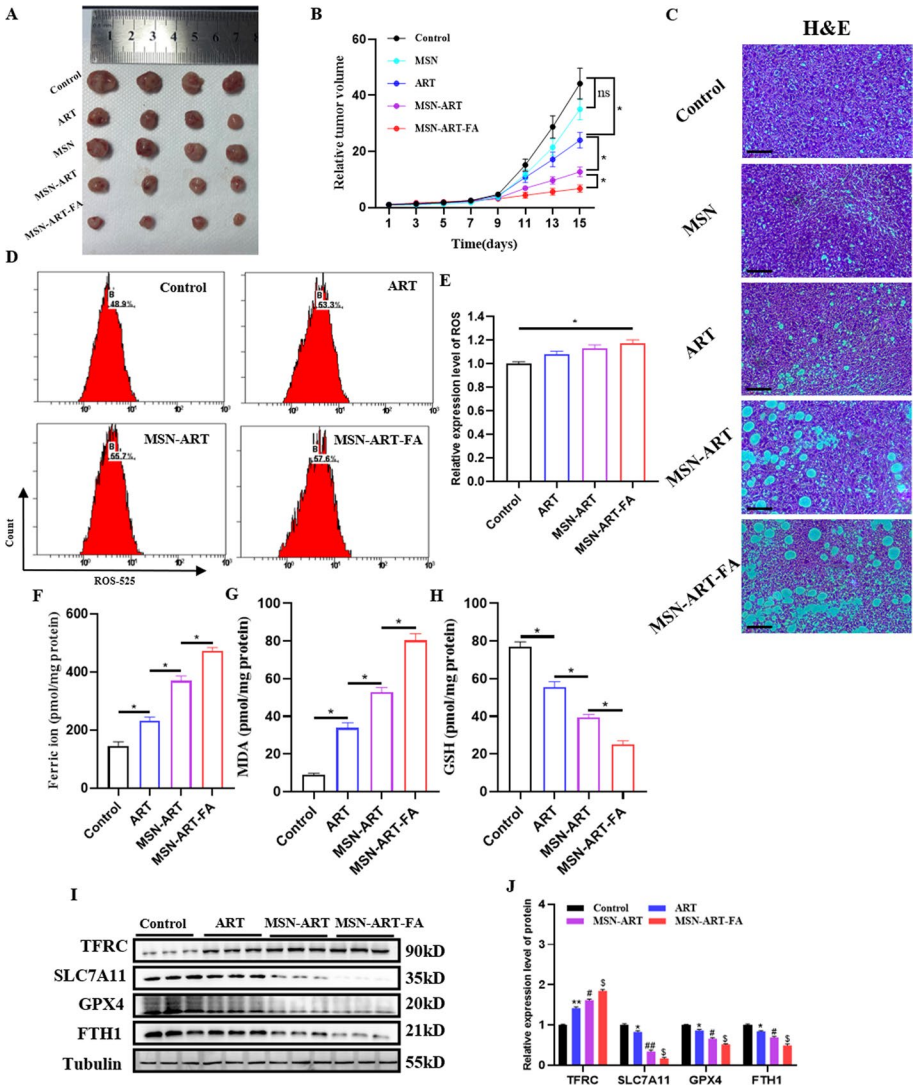

Fig. 7 MSN-ART and MSN-ART-FA enhanced ART-induced ferroptosis In vivo. **A** Image of tumor tissues after HepG2 tumor-bearing mice were killed. **B** Relative tumor volumes during treatment of HepG2 tumor-bearing mice that received saline, ART, MSN-ART or MSN-ART-FA treatments. ($n = 4$ per group, $^{*}P < 0.05$). **C** H&E images of tumor tissues (scale bar: 50 μm). **D** Fluorescence signal intensity of ROS in tumor tissues. **E** ROS level, **F** iron content, **G** MDA content and **H** GSH content in tumor tissues of HepG2 tumor-bearing mice that received saline, ART, MSN-ART or MSN-ART-FA treatments. ($n = 3$ per group, $^{*}P < 0.05$). **I** Representative immunoblots and **J** graphic representation of relative expression of TFRC, SLC7A11, GPX4, FTH1 and Tubulin in tumor tissues of HepG2 tumor-bearing mice that received saline, ART, MSN-ART or MSN-ART-FA treatments. ($n = 3$ per group, $^{*}P < 0.05$, $^{**}P < 0.01$, $^{***}P < 0.001$ compared to control, $\#P < 0.05$, $\#\#P < 0.01$ compared to ART, $\$P < 0.05$). Bars indicate mean ± SEM

control group (Fig. 8A). We performed the blood routine test and the serum biochemistry detection in above mice at the same time. Results showed that the red blood cells of control group, MSN group, ART group, MSN-ART group and MSN-ART-FA group were $(3.1 \pm 0.3) \times 10^{12}$/L, $(3.0 \pm 0.2) \times 10^{12}$/L, $(2.8 \pm 0.4) \times 10^{12}$/L, $(2.9 \pm 0.4) \times 10^{12}$/L, and $(2.7 \pm 0.5) \times 10^{12}$/L, respectively. The white blood cells were $(3.1 \pm 0.5) \times 10^{9}$/L, $(3.3 \pm 0.5) \times 10^{9}$/L, $(2.9 \pm 0.4) \times 10^{9}$/L, $(2.8 \pm 0.6) \times 10^{9}$/L, and $(3.0 \pm 0.5) \times 10^{9}$/L, respectively. The blood platelets were $(356 \pm 43) \times 10^{9}$/L, $(330 \pm 75) \times 10^{9}$/L, $(311 \pm 83) \times 10^{9}$/L, (304 ± 66)

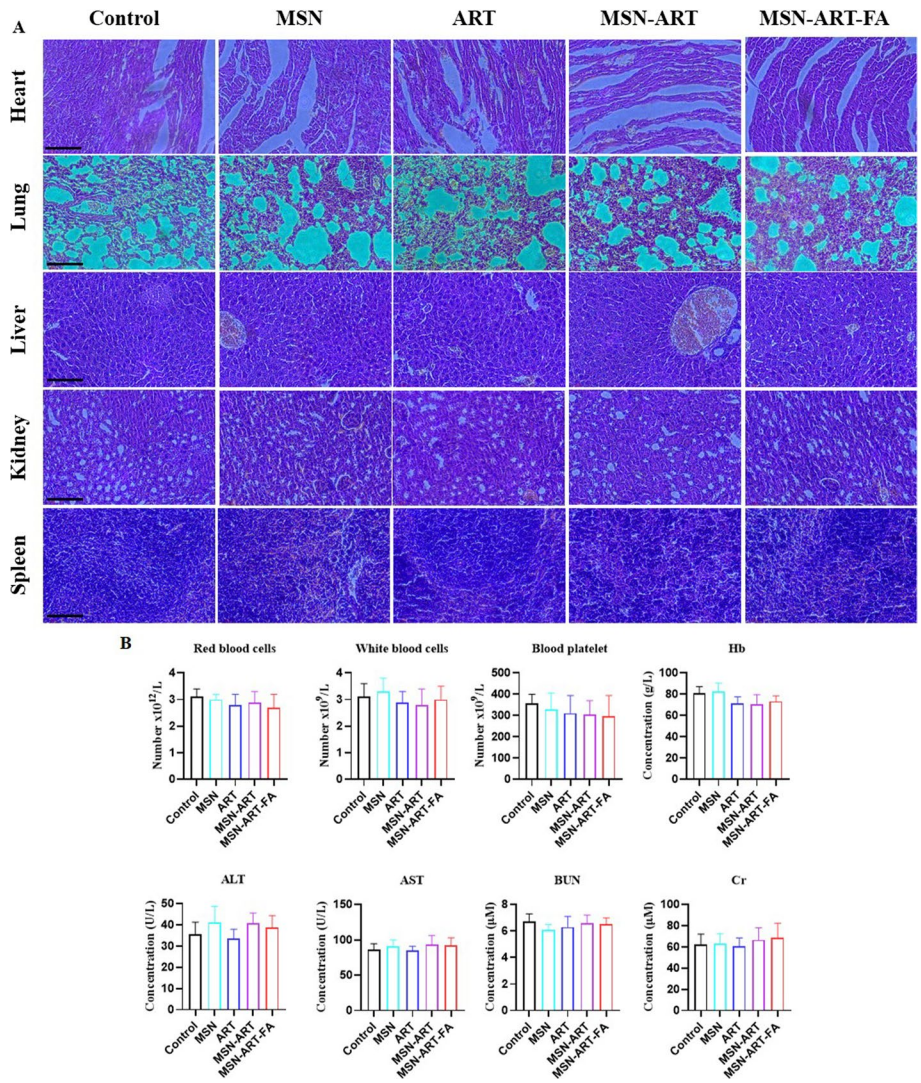

Fig. 8 MSN-ART and MSN-ART-FA had no significant toxic side effects on the critical organs. **A** HE images of heart, lung, liver, kidney and spleen tissues of HepG2 tumor-bearing mice that received saline, MSN, ART, MSN-ART or MSN-ART-FA treatments (Scale bar: 50 μm). **B** The levels of red blood cells, white blood cells, blood platelet, Hb, ALT, AST, BUN and Cr in HepG2 tumor-bearing mice that received saline, MSN, ART, MSN-ART or MSN-ART-FA treatments ($n = 4$ per group)

$\times 10^9$/L, and (297 ± 97) $\times 10^9$/L, respectively. The hemoglobin (Hb) was (80.7 ± 6.4) g/L, (82.5 ± 7.7) g/L, (71.6 ± 5.9) g/L, (70.8 ± 8.7) g/L, and (73.3 ± 5.3) g/L, respectively. The blood cells' count and Hb concentration were all within the corresponding reference values, indicating that the treatment had no significant adverse effect on bone marrow hematopoiesis. Similarly, the alanine aminotransferase (ALT) was (35.6 ± 5.7) U/L, (41.1 ± 7.6) U/L, (33.6 ± 4.3) U/L, (40.8 ± 4.8) U/L, and (38.9 ± 5.5) U/L, respectively. The glutamic-oxalacetic transaminase (AST) was (86.6 ± 7.9) U/L, (91.2 ± 8.8) U/L, (84.5 ± 6.4) U/L, (93.6 ± 12.5) U/L, and (92.2 ± 10.8) U/L, respectively. The serum urea nitrogen (BUN) was (6.7 ± 0.6) μM, (6.1 ± 0.4) μM, (6.3 ± 0.8) μM, (6.6 ± 0.6) μM, and (6.5 ± 0.5) μM, respectively. The serum creatinine (Cr) was (62.3 ± 9.8) μM, (63.1 ± 9.1) μM, (60.8 ± 7.7) μM, (66.8 ± 11.3) μM, and (68.9 ± 13.4) μM, respectively. Compared

with control group, the blood biochemical indexes were not abnormal. These results indicated that ART, MSN-ART and MSN-ART-FA had no obvious biological toxicity at the normal dose.

Moreover, we further evaluated the biotoxicity of ART and its nanomedicine in normal hepatocytes and normal mice. We selected ART, MSN-ART and MSN-ART-FA at the same dose of 160 μM (5 times dosage of IC50) ART to intervene on HL-7702 hepatocytes and found the viability of ART group was about 69.4%, although it was significantly lower than that of the control group, considering the dose factor, ART still had a good biosafety. Although the viability of MSN-ART group and MSN-ART-FA group was slightly higher than that of ART group, it was still significantly lower than that of control group. There was no significant difference in viability among ART group, MSN-ART group and MSN-ART-FA group (Additional file 1: Fig. S2A). We also performed the blood routine test and the serum biochemistry detection in normal C57BL/6J mice that received saline, MSN, ART, MSN-ART or MSN-ART-FA treatments (ART: 100 mg/kg). The results in normal C57BL/6J mice were similar to those in HepG2 tumor-bearing nude mice. The indexes of white cell, red cell, Hb, blood platelet, AST, BUN, and Cr were close in all groups, and there was no abnormality among all groups except ALT. After 7 days of high-dose ART injection, ALT in the MSN-ART-FA group showed a small and significant increase compared with the control group, but not in ART group and MSN-ART group (Additional file 1: Fig. S2B and S2C). We observed additional pathological changes of liver and kidney, the organs which are most vulnerable to the toxic side effects of drugs, but no differences were observed in all C57BL/6J mice (Additional file 1: Fig. S2D). Taken together, the nano-sized ART still had relatively good biosafety.

Discussion

The present study reported the anti-HCC effects of ART, which were evidenced via inducing ferroptosis to inhibit cell proliferation, restrain cell migration and invasion, and retard tumor growth. Traditional Chinese medicine has the characteristics of multi-target and multi-pathway in the treatment of tumor (Xiang et al. 2019). Several previous studies have indicated that ART could induce multiple modes of programmed cell death in different types of tumor cells (Chen et al. 2021; Jiang et al. 2018). A complex relationship exists between the different modes of programmed cell death. We speculate that ART for HCC treatment by no means exclusively inducing ferroptosis in hepatoma carcinoma cells, and that ART may sensitize hepatoma carcinoma cells to ferroptosis via activating signaling pathways of other programmed cell death. These speculations all need to be confirmed by a large number of studies, and we will report them further in follow-up researches.

FA plays an important role in one-carbon transfer reactions, which are involved in DNA synthesis and replication, cell division, growth, and survival, particularly in rapidly dividing cells. Therefore, FRs are highly expressed in various tumor cells to meet high FA demand of rapidly dividing cells under low FA conditions. It was reported that the binding constant of the free FA with FRs was 0.01-1 nM (Low and Kularatne 2009). However, the concentration for free FA to compete with FA-conjugated nanoparticles was 1 mM or more, suggesting that FA-conjugated nanoparticles possessed higher binding affinities to cellular FR than free FA. Taken advantage of this property, FA modification of

nanoparticles can increase retention of the nanoparticle in the tumor cells or tumor tissues and facilitate uptake of the nanoparticle by FR-mediated endocytosis, in which classical caveolae work. This enables the drug to arrive the FR-highly expressing tumor cells more efficiently and precisely. Although MSN-ART-FA had a higher uptake rate than MSN-ART in the cellular uptake fluorescence assay, we found no obviously different regulatory effects of MSN-ART and MSN-ART-FA in the detection indicators related to ferroptosis in subsequent experiments in vitro, except for ROS. Firstly, we believe that the selectivity of MSN-ART-FA for a single type of hepatoma carcinoma cell is consistent in vitro experiments, while MSN-ART could almost achieve the maximal effect of ART for 24 h co-incubation. Thence, MSN-ART-FA failed to show better result. Secondly, activation of FA receptors on hepatoma carcinoma cells is likely to contribute to ROS generation, which is worthy of further study.

Perhaps different biological effects occur when nanoparticles are used in vivo and in vitro (Bai et al. 2021a, b). MSN-ART-FA showed definitely better efficacy in tumor inhibitory rate and the detection indicators related to ferroptosis, still except for ROS, than MSN-ART in vivo. It follows then that FA modified nanoparticles can more effectively exert their value in targeting to improve anti-HCC efficacy when facing the complex tumor microenvironment and interference of various cells. The ROS assay kit purchased from Beyotime is not suitable for detecting the ROS level in tissues, which may be related to the rapid degradation of ROS after tumor tissue is stripped. Moreover, we will study the targeting of MSN-ART and MSN-ART-FA to tumor tissue and their metabolism via animal imaging technology in vivo in the future. When MSN-ART and MSN-ART-FA acted on normal hepatocytes, they showed similar killing effect as ART alone, which might be caused by the low selectivity of ART nanoparticles to normal hepatocytes. However, when MSN-ART-FA was treated in normal C57BL/6J mice, the nano-sized ART could aggravate ALT elevation response induced by high-dose ART. It was due to the relatively slow processing and rapid uptake of nanoparticles by hepatocytes possibly, which played a certain role in the accumulation of nanoparticles in the liver. Moreover, FA modification might further accelerate the uptake of ART nanoparticles by hepatocytes, thus exhibiting more severe liver damage.

The tumor microenvironment is a complex microecological region surrounding tumor cells, which can affect the initial onset, progression and metastasis of tumor from different perspectives, and is also regulated by multiple factors such as cell metabolic death, genetic epigenetic, and carcinogenic signals (Arneth 2019). Nowadays, a variety of tumor microenvironment responsive nanoparticles have been developed to treat tumors and show excellent efficacy both in vitro and in vivo (Ovais et al. 2020; Jia et al. 2020). In this study, we just used MSN as carrier of ART and selected FA to modify MSN in order to improve targeting. We suggest that ART can be loaded with tumor microenvironment responsive nanoparticles, and the bioavailability of ART can be further improved via their characteristics of drug release in tumor specific environment, so as to avoid the tolerance of ART and improve its efficacy of anti-tumor. This is a potential direction in the field of tumor therapy.

More and more clinical trial evidences show that ART has great anticancer effects on different types of cancer (Krishna et al. 2015; Hagens et al. 2019). We developed MSN-ART and MSN-ART-FA for an attempt to combine traditional Chinese medicine and

nanotechnology in HCC therapy. These results showed that MSN-ART and MSN-ART-FA had good anti-HCC effects and biosecurity, which was a very effective treatment strategy for HCC and other cancer with FR overexpressed.

Future perspectives

As a chemical extract with dose-dependent properties and multiple biological anticancer effects, ART has great potential in anticancer by inhibiting cancer cell proliferation and promoting cancer cell death through multi-target and multi-pathway. However, the mechanism of ART intervention in tumor cells and the clinical data on the use of ART in the treatment of cancer are still limited, and the drug toxicity and side effects that should be paid attention to in specific applications and the recommended drug dosage are still unclear. Ferroptosis, as a newly discovered programmed cell death mode, is of great value in anticancer research. The search for effective inducers of ferroptosis in tumor cells has attracted the attention of many scholars. We found ART could significantly induce the ferroptosis of HCC cells via increasing the level of ROS in this study. HCC cells contain a high concentration of free iron, and ART could react with free iron to generate free radicals to kill HCC cells. Previous studies have shown that ART-induced intracellular ROS elevation is widespread. Thus, we believe that ART can induce ferroptosis not only in HCC cells, but also in other tumor cells, which needs to be supported by subsequent studies.

ART is very difficult to dissolve in water, resulting in its low bioavailability and inapparent efficacy. In recent years, nanomedicine technology has developed rapidly, and a series of nanomedicine have been developed and gradually entered the clinical trial stage. In this study, we synthesized ART nanomedicine to solve the above clinical problems of ART via reducing biotoxicity, improving bioavailability and tumor-targeting performance. Considering the metabolism and excretion mode of nanomedicine, the current challenge in clinical application is the evaluation of biosafety. We conducted studies of ART and its nanomaterials at the cellular and animal levels to determine the relatively safe and effective dose for HCC treatment and a portion of its pharmacological and toxicological mechanisms. We believe that this achievement will provide more scientific basis for ART and its nanomaterials against HCC, further promote the broad-spectrum anti-tumor clinical research of ART, and contribute its own important value to the clinical development of ART.

Conclusion

In conclusion, this study demonstrated that, on the one hand, ART could induce ferroptosis in hepatoma carcinoma cells. On the other hand, developed MSN-ART and MSN-ART-FA could improve bioavailability of ART to enhance ferroptosis, thereby inhibiting cell proliferation, migration and invasion in vitro. Especially, MSN-ART-FA could further retard tumor growth by virtue of its excellent targeting in vivo. It provided technical and theoretical support for the treatment of HCC and also broadened the field of vision for clinical treatment of other cancers.

Supplementary Information

The online version contains supplementary material available at https://doi.org/10.1186/s12645-023-00232-4.

Additional file 1: Figure S1. Characterization of ART in MSN-ART using HPLC. **Table S1.** Sample concentration data of ART in MSN-ART. **Figure S2.** MSN-ART and MSN-ART-FA had no significant toxic side effects on human normal hepatocyte and the critical organs of C57BL/6J mice.

Acknowledgements
Thank Han Zhang for her contribution to article writing and project design.

Author contributions
DN designed this project and wrote the original draft; TG and YZ drafted the manuscript; MS conducted the flow cytometry experiment; MY, XZ and WL drew the chart. ML was responsible for the overall direction of the paper and for editing to the manuscript.

Funding
This work was supported by the National Natural Science Foundation of China (81571797), the Natural Science Foundation of Nanjing University of Chinese Medicine China, (XZR2020093), the 333 Plan Foundation of Jiangsu, China (Jiangsu Talent Office [2022]21-2) and Taizhou People's Hospital Medical Innovation Team Foundation, China (CXTDA201901).

Availability of data and materials
The datasets generated during and/or analyzed during the current study are available from the corresponding author on reasonable request.

Declarations

Ethics approval and consent to participate
The Institutional Animal Care and Use Committee of the Jiangsu Huachuang Xinuo Medical Technology Co., LTD approved all of the procedures performed in this study (Approval Number: IACUC-2022-0010).

Consent for publication
All authors approved the final manuscript and the submission to ***Cancer Nanotechnology***.

Competing interests
The authors declare no competing interests.

Received: 5 May 2023 Accepted: 11 October 2023
Published online: 21 October 2023

References

Arneth B (2019) Tumor microenvironment. Medicina (Kaunas Lithuania) 56(1):15
Bai G, Gao Y, Liu S et al (2021a) pH-dependent rearrangement determines the iron-activation and antitumor activity of artemisinins. Free Radic Biol Med 163:234–242
Bai X, Wang J, Mu Q et al (2021b) *In vivo* protein corona formation: characterizations, effects on engineered nanoparticles' biobehaviors, and applications. Front Bioeng Biotechnol 9:646708
Berköz M, Özkan-Yılmaz F, Özlüer-Hunt A et al (2021) Artesunate inhibits Melanoma progression *in vitro* via suppressing STAT3 signaling pathway, pharmacological reports. PR 73(2):650–663
Capelletti MM, Manceau H, Puy H et al (2020) Ferroptosis in liver diseases: an overview. Int J Mol Sci 21(14):4908
Chekem L, Wierucki S (2006) Extraction of artemisinin and synthesis of its derivates artesunate and artemether. Medecine tropicale revue du Corps de sante colonial 66(6):602-5
Chen Y, Wang F, Wu P et al (2021) Artesunate induces apoptosis, autophagy and ferroptosis in diffuse large B cell Lymphoma cells by impairing STAT3 signaling. Cell Signal 88:110167
Eling N, Reuter L, Hazin J et al (2015) Identification of artesunate as a specific activator of ferroptosis in pancreatic cancer cells. Oncoscience 2(5):517–532
Farran B, Pavitra E, Kasa P et al (2019) Folate-targeted immunotherapies: passive and active strategies for cancer. Cytokine Growth Factor Rev 45:45–52
Hu W, Zhou C, Jing Q et al (2021a) FTH promotes the proliferation and renders the HCC cells specifically resist to ferroptosis by maintaining iron homeostasis. Cancer Cell Int 21(1):709
Hu X, Zhang J, Deng L et al (2021b) Galactose-modified PH-sensitive Niosomes for controlled release and hepatocellular carcinoma target delivery of Tanshinone IIA. AAPS PharmSciTech 22(3):96
Hwang S, Lee SG, Belghiti J (2010) Liver transplantation for HCC: its role: eastern and western perspectives. J Hepato-Biliary-Pancreat Sci 17(4):443–448
Ikeda M, Morizane C, Ueno M et al (2018) Chemotherapy for hepatocellular carcinoma: current status and future perspectives. Jpn J Clin Oncol 48(2):103–114
Jia N, Li W, Liu D et al (2020) Tumor microenvironment stimuli-responsive nanoparticles for programmed anticancer drug delivery. Mol Pharm 17(5):1516–1526
Jiang F, Zhou JY, Zhang D et al (2018) Artesunate induces apoptosis and autophagy in HCT116 colon cancer cells, and autophagy inhibition enhances the artesunate–induced apoptosis. Int J Mol Med 42(3):1295–1304
Krishna S, Ganapathi S, Ster IC, Randomised A et al (2015) Double blind, placebo-controlled pilot study of oral artesunate therapy for colorectal cancer. EBioMedicine 2(1):82–90

Kumar P, Huo P, Liu B (2019) Formulation strategies for folate-targeted liposomes and their biomedical applications. Pharmaceutics 11(8):381
Lee HY, Nga HT, Tian J et al (2021) Mitochondrial metabolic signatures in hepatocellular carcinoma. Cells 10(8):1901
Li H, Xu K, Pian G et al (2019) Artesunate and sorafenib: combinatorial inhibition of liver cancer cell growth. Oncol Lett 18(5):4735–4743
Low PS, Kularatne SA (2009) Folate-targeted therapeutic and imaging agents for cancer. Curr Opin Chem Biol 13(3):256–262
Mou Y, Wang J, Wu J et al (2019) Ferroptosis, a new form of cell death: opportunities and challenges in cancer. J Hematol Oncol 12(1):34
Ovais M, Mukherjee S, Pramanik A et al (2020) Designing stimuli-responsive upconversion nanoparticles that exploit the tumor microenvironment. Adv Mater (Deerfield Beach Fla) 32(22):e2000055
Park DH, Cho J, Kwon OJ et al (2016) Biodegradable inorganic nanovector passive versus active tumor targeting in siRNA transportation. Angewandte Chemie 55(14):4582–6
Song Q, Peng S, Che F et al (2022) Artesunate induces ferroptosis via modulation of p38 and ERK signaling pathway in glioblastoma cells. J Pharmacol Sci 148(3):300–306
Tang Y, Wang X, Li J et al (2019a) Overcoming the Reticuloendothelial System Barrier to Drug Delivery with a don't-Eat-Us strategy. ACS Nano 13(11):13015–13026
Tang H, Chen D, Li C et al (2019b) Dual GSH-exhausting sorafenib loaded manganese-silica nanodrugs for inducing the ferroptosis of hepatocellular carcinoma cells. Int J Pharm 572:118782
Tang H, Li C, Zhang Y et al (2020) Targeted manganese doped silica nano GSH-cleaner for treatment of liver cancer by destroying the intracellular redox homeostasis. Theranostics 10(21):9865–9887
von Hagens C, Walter-Sack I, Goeckenjan M et al (2019) Long-term add-on therapy (compassionate use) with oral artesunate in patients with metastatic Breast cancer after participating in a phase I study (ARTIC M33/2. Phytomed Int J Phytother Phytopharmacol 54:140–148
Wang N, Zeng GZ, Yin JL et al (2019) Artesunate activates the ATF4-CHOP-CHAC1 pathway and affects ferroptosis in Burkitt's Lymphoma. Biochem Biophys Res Commun 519(3):533–539
Xiang Y, Guo Z, Zhu P et al (2019) Traditional Chinese medicine as a cancer treatment: modern perspectives of ancient but advanced science. Cancer Med 8(5):1958–1975
Yang S, Wang Z, Ping Y et al (2020) PEG/PEI-functionalized single-walled carbon nanotubes as delivery carriers for doxorubicin: synthesis, characterization, and *in vitro* evaluation. Beilstein J Nanotechnol 11:1728–1741
Yang X, Zheng Y, Liu L et al (2021) Progress on the study of the anticancer effects of artesunate. Oncol Lett 22(5):750
Zhou S, Jin J, Wang J et al (2021) Effects of breast cancer genes 1 and 2 on cardiovascular diseases. Curr Probl Cardiol 46(3):100421
Zhu Y, Yue M, Guo T et al (2021) PEI-PEG-Coated mesoporous silica nanoparticles enhance the antitumor activity of tanshinone IIA and serve as a gene transfer vector. Evidence Based Complement Andalternat Med ECAM 2021:6756763

Publisher's Note